JOURNAL OF MATERIALS SCIENCE 27 (1992) 3050–3061

Temperature–enthalpy approach to the modelling of self-propagating combustion synthesis of materials

A. K. BHATTACHARYA
Material Science and Technology Division, Los Alamos National Laboratory, Los Alamos, NM 87545, USA

A new temperature–enthalpy approach has been proposed to model self-propagating combustion synthesis of advanced materials. This approach includes the effect of phase change which might take place during a combustion process. The effect of compact porosity is also modelled based on the conduction, convection and radiation in the local scale. Various parametric studies are made to analyse numerically the effects of activation energy, non-reacting phase content, porosity, Biot number, etc. The model predictions of the combustion pattern are in close agreement with those observed in experiments.

Nomenclature

c = Concentration (wt %)
B_i = Biot number = hL/k
f = Fractional value
c_p = Specific heat (J kg^{-1} K)
h = Heat-transfer coefficient (W m^{-2} K)
L = Height of material, m
Q = Heat of reaction (J kg^{-1})
ΔH^*_{SL} = Latent heat of fusion (J kg^{-1})
ΔH^*_{SE} = Latent heat of fusion at eutectic (J kg^{-1})
k = Thermal conductivity (W m^{-1} K)
k' = Equilibrium partition coefficient
ϕ = Reaction kinetic function
t = Time (s)
τ = Non-dimensional time
T = Temperature (K)
T_0 = Initial temperature (K)
θ = Non-dimensional temperature
H = Enthalpy (J kg^{-1})
Φ = Kinetic function
ϕ' = Non-dimensional enthalpy
v_f = Volume fraction of non-reactive phase
V = Volume (m^3)
k_0 = Pre-exponential constant to reaction rate (s^{-1})
z = Cartesian co-ordinate
z^* = Non-dimensional co-ordinate
η = Non-dimensional reacted fraction
ρ = Density (kg m^{-3})
φ = A non-dimensional temperature
ε = Pore surface emissivity
σ = Planck's constant

Subscript
i Initial state
r Reacted state
l, L Liquid state
s Solid state
E Eutectic
M Melting point of pure material
P Centre of control volume
s Southern side of central volume
S Southern control volume
n Northern side of central volume
N Northern control volume

Superscript
* Non-dimensional term
n New time level
o Old time level
m Iteration level

1. Introduction

Self-propagating combustion or reaction synthesis is becoming increasingly popular as a novel material processing technique for the production of advanced ceramics, intermetallics and their compounds [1–4]. In this process, self-sustaining highly exothermic solid-state reactions result in a combustion wave, and as the combustion wave propagates through a compacted mixture of appropriate reactant powders, the reactants are converted to a desired product. It has been claimed that this process has various advantages including higher purity of the products [5] and elimination of any high-temperature furnaces, which gives rise to low energy requirements. Also, a possible reduction in reinforcement/matrix interfacial reaction can be anticipated because of quick processing time.

The nature of propagation of a combustion wave through a compacted reactant mixture is governed by heat-transfer characteristics and thermophysical criteria of the mixture reaction. Thus a major concern in

* *Present address*: Max Planck Institute für Metallforschung, D-7000 Stuttgart 1, Germany.

0022–2461

the theoretical study of combustion synthesis is the determination of conditions under which steady-state reaction-wave propagation exists. Under such steady-state conditions, the combustion wave virtually propagates at a constant velocity. However, such conditions depend on various material parameters, such as heat of reaction; activation energy; porosity of compact etc. in a very sensitive way. It has been observed [6–8] that even slight changes in some of these parameters may cause different modes of combustion, including instability and extinction as the two extreme cases. Existence of various modes of these kinds results in products that are homogeneous, layered, partially reacted and so on.

There is much combustion-related literature on the propagation of fronts in reacting systems, and a number of theoretical studies exist on wave propagation behaviour in solid–solid combustion synthesis. The basic energy equations in all of these treatments are developed and numerically solved in terms of temperature as the sole dependent variable [6, 9, 10]. Merzhanov and Khaikin [6] have presented an excellent comprehensive theoretical description on combustion synthesis with major emphasis on the steady-state behaviour of combustion process. Hlavacek and co-workers [9, 10] have modelled an exothermic reaction system and numerically analysed the temperature history in the material. They have also made an elaborate study of the stability behaviour of such a combustion front. However, when applied to a combustion problem there are two major shortcomings in these approaches. Firstly, any phase-change effect is neglected; and secondly, because of the possibility of a very steep reaction front, the temperature gradient can be so high as to create substantial numerical difficulties. Also, various microstructural effects including porosity and pore size of the compact, and the effect of reinforcing phases (if any) have not been considered. The objective of the present work has been to present a new formulation of a solid–solid combustion process so that the above difficulties can be addressed. In this paper a temperature–enthalpy approach has been taken to formulate the combustion process as typically encountered in self-propagating high-temperature synthesis of advanced ceramics, intermetallics and their composites. The treatment is quite general in nature, so that it may be applicable to any relevant material system.

2. Mathematical formulation

The present work is mainly concerned with the treatment of solid–solid non-catalytic reactions in a compacted powder mass, in terms of enthalpy and temperature as the two dependent variables. This approach conveniently allows us to take into account the variable thermal properties, insofar as they can be regarded as functions of temperature only, and also the effect of phase changes that may take place during the combustion process. We also consider the effects of porosity and temperature on the local thermal conductivity, k. Thus, the general energy equation for a reacting system may be written as

$$\rho c_p \frac{\partial T}{\partial t} = \nabla^2(kT) + \rho(1 - v_f)Q\phi(\eta, T) \quad (1)$$

where ρ is the average density of the compact with due consideration to the effects of porosity and properties of various powder contents; c_p is the specific heat; k is the local thermal conductivity; Q is the heat of reaction, v_f is the volume fraction of any non-reactive phase content (e.g. reinforcing agent etc); ϕ is the kinetic term related to the type of reaction; and η is the reacted fraction to be described in terms of species concentration c. This paper considers only the one-dimensional situation in terms of the spatial co-ordinate z, as shown schematically in Fig. 1. It will be assumed that during a reaction the condensed products are formed from the initial condensed reactant and the kinetic function $\phi(\eta; T)$ can be written as

$$\phi(\eta, T) = k_0\Phi(\eta)\exp\left(-\frac{E}{RT}\right) \quad (2)$$

Dusinberre [11] introduced the enthalpy method to model the transient heat-flow problem, which has been later adopted by various authors [12–14] in modelling solidification problems by treating the solid–liquid region as a continuum with properties varying with fraction liquid, solid or a mushy phase containing both solid and liquid. By adopting procedures along the same lines, we first represent the basic equation in terms of temperature and enthalpy. This permits us later to incorporate the non-linear latent heat release through non-linear variation of the liquid fraction. Thus Equation 1 becomes

$$\rho\frac{\partial H}{\partial t} = \frac{\partial}{\partial x}\left(k\frac{\partial T}{\partial x}\right) + \rho(1 - v_f)Qk_0\Phi(\eta)\exp\left(-\frac{E}{RT}\right) \quad (3)$$

Here, the enthalpy H has been introduced to the transient term. A binary phase diagram containing an

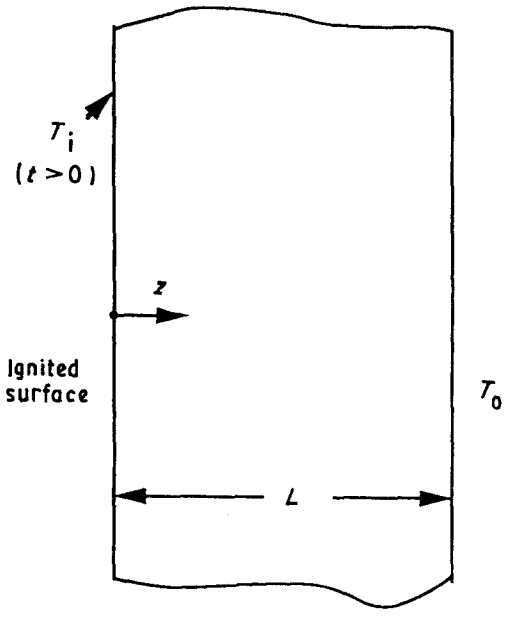

Figure 1 Schematic representation of co-ordinate system used for analysis.

eutectic is considered to describe a typical reaction process between two solid materials A and B. Physically speaking, this reaction may involve different phases during the reaction process in the following four regions: (i) Solid phase, product is below the solidus line; (ii) eutectic phase, product can have liquid eutectic and posteutectic solid; (iii) mushy phase, product can have posteutectic liquid and solid; (iv) liquid phase, product is above the liquidus line. The relationship between temperature and enthalpy in these four regions is as follows:

$$\begin{aligned}
&\text{Solid phase, } H = c_{pr}T, && T < T_E\\
&\text{Eutectic phase, } H = c_{pr}T + f_{lE}\Delta H_{SE}, && T = T_E\\
&\text{Mushy phase, } H = c_{pr}T + f_l\Delta H_{SL}, && T_E < T \leqslant T_L\\
&\text{Liquid phase, } H = c_{pl}T + \Delta H_{SL}, && T > T_L
\end{aligned} \tag{4}$$

In the above description, c_{pr} in the mushy zone includes the appropriate effects of both solid- and liquid-phase content. We also assume that the average thermal conductivity and specific heat for the reacted and unreacted solids are the same. Hence the temperature–enthalpy relationship is the same for both. The fraction of liquid at any temperature is given by the Scheil equation [15] as

$$f_l = (\varphi)^{-\frac{1}{(1-k')}} \tag{5}$$

where φ is an appropriate non-dimensional temperature reflecting liquidus and melting temperature, and k' is the equilibrium partition coefficient. The weight fraction f_E of the eutectic is determined by the equation

$$f_E = \left(\frac{c_E}{c_0}\right)^{-\frac{1}{(1-k')}} \tag{6}$$

where c_0 and c_E are the initial and eutectic solute contents, respectively.

We consider here that the reactant A is in excess of reactant B, so that the reaction process can be described as a first-order reaction and thus the function $\Phi(\eta)$ in Equation 2 can be expressed as

$$\Phi(\eta) = c_0(1 - \eta) \tag{7}$$

where c_0 is the initial concentration and $\eta = 1 - c/c_0$. To evaluate η we will take resort to the mass balance equation which, in the present case, is given by

$$\frac{\partial c}{\partial t} = -k_0 c \exp\left(-\frac{E}{RT}\right) \tag{8}$$

Equations 3–8 thus describe a typical combustion process and can be solved with appropriate initial and boundary conditions. We can non-dimensionalize the governing Equations 3, 4 and 8 using the following reference values of enthalpy and temperature:

$$\begin{aligned}
\phi' &= \frac{1}{\rho v}\int_v \frac{\rho(H - H^*_{SE})}{\Delta H^*_{SL}}\,dv = \frac{H - H^*_{SE}}{\Delta H^*_{SL}}\\
\theta &= \frac{c_{pr}(T - T_E)}{\Delta H^*_{SL}}
\end{aligned} \tag{9}$$

where $H^*_{SE} = c_{pr}(T_E - T_0)$.

We also use the following non-dimensionalization

$$k^* = \frac{k}{k_s},\ z^* = \frac{z}{H},\ \tau = \frac{tk_s}{H^2\rho c_{pr}} \tag{10}$$

The transformed energy Equation 3 thus becomes

$$\frac{\partial\phi'}{\partial\tau} = \frac{\partial^2(k^*\theta)}{\partial z^{*2}} + (1 - v_f)\gamma\nu(1 - \eta) \times \exp\left(-\frac{1}{N + \beta\theta}\right) \tag{11}$$

where the dimensionless reaction parameters γ, ν, N and β have been defined as

$$\begin{aligned}
\gamma &= \left(\frac{Q}{\Delta H^*_{SL}}\right)\\
\nu &= (k_0H^2)\left(\frac{\rho c_{pr}}{k_s}\right)\\
N &= \left(\frac{RT_E}{E}\right)\\
\beta &= \left(\frac{R}{c_{pr}}\right)\left(\frac{\Delta H^*_{SL}}{E}\right)
\end{aligned} \tag{12}$$

The non-dimensional relationships between enthalpy and temperatures in various phase zones are derived from Equation 4 in the following manner.

$$\text{Solid phase, } \phi' = \theta = \frac{c_{pr}(T - T_E)}{\Delta H^*_{SL}},\ \phi' \leqslant 0 \tag{13}$$

$$\begin{aligned}
&\text{Eutectic phase, } \phi' = f_{lE}\frac{\Delta H^*_{SE}}{\Delta H^*_{SL}}\\
&\theta = 0\\
&0 \leqslant \phi' \leqslant f_E\frac{\Delta H^*_{SE}}{\Delta H^*_{SL}} \quad \text{and} \quad 0 \leqslant f_{lE} \leqslant f_E
\end{aligned} \tag{14}$$

$$\begin{aligned}
&\text{Mushy phase, } \phi' = f_l + \frac{c_{pl}(T - T_E)}{\Delta H^*_{SL}}\\
&\theta = (\phi' - f_l)\frac{c_{pr}}{c_{pl}}\\
&f_l = \left[\frac{T_M - T_E}{T_M - T_L} - \frac{\Delta H^*_{SL}}{c_{pr}(T_M - T_E)}\theta\right]^{-\frac{1}{(1-k')}}\\
&k = k_s(1 - f_l) + k_l f_l\\
&f_E \leqslant \phi' \leqslant \left(1 + \frac{c_{pl}(T_L - T_E)}{\Delta H^*_{SL}}\right)
\end{aligned} \tag{15}$$

$$\begin{aligned}
&\text{Liquid phase, } \phi' = 1 + \frac{c_{pl}(T - T_E)}{\Delta H^*_{SL}}\\
&\theta = (\phi' - 1)\frac{c_{pr}}{c_{pl}}\\
&\phi' > \left(1 + \frac{c_{pl}(T_L - T_E)}{\Delta H^*_{SL}}\right)
\end{aligned} \tag{16}$$

The mass balance Equation 8, when appropriately transformed, becomes

$$\frac{\partial\eta}{\partial\tau} = \nu(1 - \eta)\exp\left(-\frac{1}{N + \beta\theta}\right) \tag{17}$$

The porosity of the powder compact will have an important effect on the average density ρ and the thermal conductivity k. The density at a porosity p is given as $\rho = \rho_S(1 - p)$, where ρ_S is the solid density at zero porosity which can be considered as the average of the powder mixture. For calculating the effect of porosity on the thermal conductivity, we make a simplifying assumption that the mixed powder particles, including reinforcing inert particles (if any), can be approximated to have an average diameter which is uniform throughout the compact. For simplifying calculations, we also assume that after cold compaction the powder particles are stacked up as shown in Fig. 2a, showing that the particles are squeezed uniformly [16]. The transport of heat through a porous compact occurs by a combination of conduction, convection and radiation. Their cumulative effect can be represented by an overall local thermal conductivity k_e which should be considered for thermal conductivity k^* in Equation 11. The modelling of overall thermal conductivity in a compact powder mass has been reported elsewhere [16, 17]. Here, the geometry of the compact has been modelled as in Fig. 2a and b, with the simplification that the pores have a single characteristic size v, and that all pores are evenly spaced by a distance l perpendicular to the heat-flow direction. The effective conductivity can then be expressed as [16]

$$k^* = \frac{k_e}{k_s} = \frac{\chi + \Gamma\left(1 + \frac{1}{\delta}\right) + 1}{\chi + \frac{\Gamma}{\delta} + (1 + \Gamma)\Big/\left(\frac{4\varepsilon\sigma v\bar{T}^3}{k_s} + \frac{k_p}{\mu k_s}\right)} \quad (18)$$

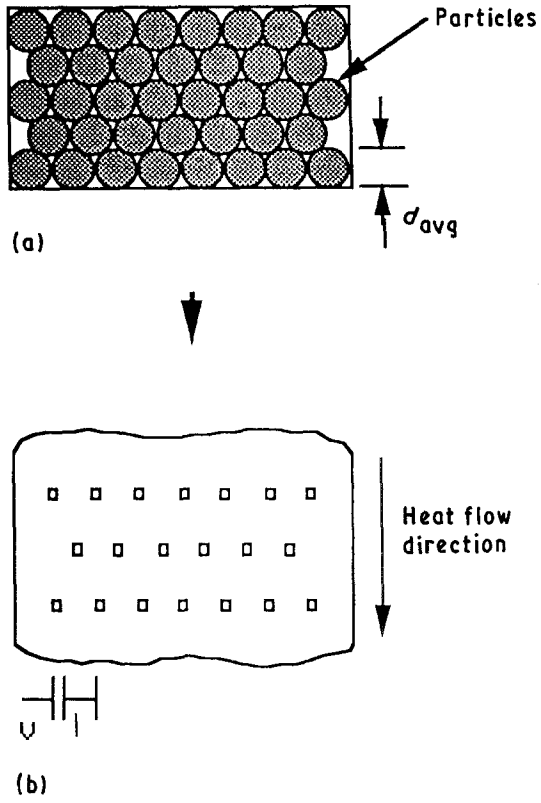

Figure 2 Transformed model representation of a compact in terms of solid powder and isolated regular arrays of closed pores.

where $\bar{T}$ is the average temperature of pore surface, and

$$\delta = \frac{v}{l} = \frac{p^{1/3}}{1 - p^{1/3}}$$

$$\chi = \frac{(1 + \delta)\left[\left(\frac{2 + \delta}{1 + \delta}\right)\ln(1 + \delta) + 1\right]}{\delta \ln(1 + \delta)}$$

$$\Gamma = 1 + \frac{1}{\ln\left(1 + \frac{1}{\delta}\right)} \quad (19)$$

where ε and σ are the emissivity of the pore surface and Planck's constant, respectively. k_p is the thermal conductivity of the pore fluid, and μ is an adjustable parameter that relates the conduction across the pores to the local conductivity of the solid. It is reasonable to approximate the average pore temperature $\bar{T}$ as the local temperature T in the compact. Equation 18 can then be rewritten in a fully non-dimensionalized form as

$$k^* = \frac{k_e}{k_s} = \frac{\chi + \Gamma\left(1 + \frac{1}{\delta}\right) + 1}{\chi + \frac{\Gamma}{\delta} + (1 + \Gamma)\Big/\left[\Omega\left(1 + \frac{\Delta H^*_{SL}}{c_{pr}T_E}\theta\right) + \frac{k_p}{\mu k_s}\right]} \quad (20)$$

where $\Omega = 4v\varepsilon\sigma T_E^3/k_s$ is a pore-size-dependent parameter and reflects the relative importance between thermal conductivity due to radiation and thermal conductivity of the solid powder. The effect of non-reacting reinforcing phases which may be used for synthesizing a composite, e.g. Ti + C + SiC, is considered through the volume fraction term v_f and also by appropriately modifying the thermal conductivity k_s and solid density ρ_s of the powders.

3. Numerical solution

The propagation of the reaction front in the porous compact is represented by the governing non-linear Equations 11 and 17, along with appropriate initial and boundary conditions which will be described later when we consider a specific example. These equations have been solved by using the control volume formulation of finite difference equations. The initial step in obtaining a finite difference representation is to subdivide the region of interest (only the z-variable in the present case) into a number of small elements. Then nodal points are placed at the centre of each element and the values of the enthalpy, ϕ', and temperature, θ, at these nodes are calculated as functions of time, τ.

Integrating the energy equation over a volume element shown in Fig. 3, we obtain the following finite

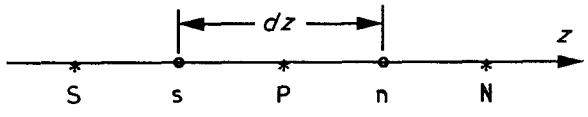

Figure 3 Schematic representation of a typical control volume in z-co-ordinate system with given positive direction for computational scheme.

difference equation for the control volume, P, where subscript is used to denote node location, and superscripts n and o are used to denote new and old time steps, respectively

$$a_P^o\phi_P'^n + a_P\theta_P^n - (1 - v_f)v\gamma(1 - \eta) \times \exp\left(-\frac{1}{N + \beta\theta_P^n}\right) = RHS \quad (21)$$

where

$$RHS = d_s\theta_S^n + d_n\theta_N^n + a_P^o\phi_P'^o$$

$$a_P^o = \frac{1}{\Delta\tau}$$

$$d_s = \frac{k_s^*}{(z_n - z_s)(z_P - z_S)}$$

$$d_n = \frac{k_n^*}{(z_n - z_s)(z_N - z_P)}$$

k^* in these equations is obtained from Equation 20 by considering appropriate porosity and pore size.

The finite difference Equation 21 at all node points is solved by using the Gauss–Seidel iterative technique. This method was selected because the iterations necessary for the solution and the iterations necessary to ascertain the appropriate ϕ'–θ relationship in various phases could be carried out simultaneously. Also, the method needs very little computer memory due to its specific iterative nature. Once the solution at a time level is obtained, the initial solution of the new time level is set equal to that of the old one and a new transient iteration is started. At the same time, the left hand side of Equation 21 is updated based on the following ϕ'–θ relationships at the appropriate phase zones.

In solid zone (below eutectic), $RHS < 0$; $\theta_P^n = \phi_P'^n$

$$(a_P^o + a_P)\phi_P'^n - (1 - v_f)v\gamma(1 - \eta) \times \exp\left(-\frac{1}{N + \beta\phi_P'^n}\right) = RHS \quad (22)$$

In eutectic zone

$$0 \leqslant RHS < \left[a_P^o f_E \frac{\Delta H_{SE}^*}{\Delta H_{SL}^*} - (1 - v_f)v\gamma(1 - \eta)\exp\left(-\frac{1}{N}\right)\right]$$

$$\theta_P^n = 0$$

$$\phi_P'^n = \frac{1}{a_P^o}\left[RHS + (1 - v_f)v\gamma(1 - \eta)\exp\left(-\frac{1}{N}\right)\right] \quad (23)$$

In mushy zone

$$\left[a_P^o f_E \frac{\Delta H_{SE}^*}{\Delta H_{SL}^*} - (1 - v_f)v\gamma(1 - \eta)\exp\left(-\frac{1}{N}\right)\right] \leqslant RHS$$

$$< \left\{ a_P^o\left[1 + \frac{c_{pl}(T_L - T_E)}{\Delta H_{SL}^*}\right] + a_P\frac{c_{pr}(T_L - T_E)}{\Delta H_{SL}^*} - (1 - v_f)v\gamma(1 - \eta)\exp\left[-\frac{1}{N + \beta\dfrac{c_{pr}(T_L - T_E)}{\Delta H_{SL}^*}}\right] \right\}$$

$$\phi_P'^n = f_l + \frac{c_{pl}}{c_{pr}}\theta_P^n$$

$$\left(a_P^o + a_P\frac{c_{pr}}{c_{pl}}\right)\left(f_l + \frac{c_{pl}}{c_{pr}}\theta_P^n\right) - (1 - v_f)v\gamma(1 - \eta)\exp\left(-\frac{1}{N + \beta\theta_P^n}\right) - a_P f_l\frac{c_{pr}}{c_{pl}} = RHS$$

$$f_l = \left[\frac{T_M - T_E}{T_M - T_L} - \frac{\Delta H_{SL}^*}{c_{pr}(T_M - T_L)}\theta_P^n\right]^{\frac{1}{1-k'}}$$

$$k = k_s(1 - f_l) + k_l f_l \quad (24)$$

In liquid zone

$$RHS > \left\{ a_P^o\left[1 + \frac{c_{pl}(T_L - T_E)}{\Delta H_{SL}^*}\right] + a_P\frac{c_{pr}(T_L - T_E)}{\Delta H_{SL}^*} - (1 - v_f)v\gamma(1 - \eta)\exp\left[-\frac{1}{N + \beta\dfrac{c_{pr}(T_L - T_E)}{\Delta H_{SL}^*}}\right] \right\}$$

$$\theta_P^n = (\phi_P'^n - 1)\frac{c_{pr}}{c_{pl}}$$

$$\left(a_P^\circ + a_P \frac{c_{pr}}{c_{pl}}\right)\phi_P'^n - (1 - v_f)v\gamma(1 - \eta)\exp\left[-\frac{1}{N + \beta\dfrac{c_{pr}}{c_{pl}}(\phi_P'^n - 1)}\right] - a_P\frac{c_{pr}}{c_{pl}} = RHS \quad (25)$$

Equations 22–25 provide the relationship of θ_P^n and $\phi_P'^n$ in the various phases. Except for Equation 23, all these equations contain θ_P^n or $\phi_P'^n$ in a highly non-linear way. These equations are solved for $\phi_P'^n$ in Equations 22 and 25 by using the Regula–Falsi method. From the values obtained for $\phi_P'^n$, θ_P^n are calculated. In Equation 24, θ_P^n and f_l are solved simultaneously by using the same method, and then from these values $\phi_P'^n$ is calculated. Although Equation 17 for η is coupled with Equation 11 for ϕ' and θ, we could decouple it to reduce complexity in the analyses by considering η values of the previous step as the approximation of η values in the current step. Then from Equation 17, with appropriate initial conditions, we can write η as

$$\eta = 1 - \exp\left[\int_0^\tau -v\exp\left(-\frac{1}{N + \beta\theta_P^\circ}\right)d\tau\right] \quad (26)$$

The process of transient iteration is repeated for all nodes and the recorded changes in ϕ' values relative to the first guesses are examined to see if they satisfy a 'relative error' criterion separately at every node point which is defined as

$$\left|\frac{\phi'^{m+1} - \phi'^m}{\phi'^m}\right| \leqslant 0.00001 \quad (27)$$

where m is the mth iteration in the current time step. The "residual norm" criterion which is based on the residues of the finite difference Equation 21 was also checked at all control volumes. For all practical purposes, in the present calculation solutions with reasonable accuracy were obtained by satisfying criteria in Equation 27 alone, and hence only this criterion was used for all calculations reported here. Because of the non-linear nature of the algebraic equations, the question of numerical stability was also examined by numerical experimentation with various combinations of spatial and time steps. Instability was never encountered, and a time step of 0.005 and spatial step of 0.01 were found to be accurate enough to provide satisfactory results with good convergence.

4. Results and discussion

The temperature–enthalpy model developed here and the numerical calculation procedure described above were employed to obtain sets of results for various types of parametric values. A specific example of TiC combustion synthesis has been considered and the relevant physical properties of TiC used for the calculation are indicated in Table I for a compact of length 0.1 m. With reference to the Ti–C phase diagram [18] (Fig. 4), we consider the Ti:C ratio as 50:50 for the present calculation. The use of this composition in the present calculation demonstrates the generality of this approach for considering compositional varieties that may be present while synthesizing a particular powder mixture. It is possible to look at the effect of stoichiometry on the combustion process by reading the binary diagram for a particular composition and appropriately calculating f_E in Equation 6. The following two non-dimensionalized boundary conditions Equation 28a and an initial condition Equation 28b have been considered for obtaining the necessary solutions of the governing equations

TABLE I Relevant thermo-physical properties related to the reaction Ti + C = TiC.

Heat of reaction, Q	3070 kJ kg^{-1}
Adiabatic reaction temperature, T_a	3290 K
Activation energy, E	117 kJ mol^{-1}
Latent heat of fusion, ΔH_{SL}^*	1400 kJ kg^{-1}
Melting temperature of pure material, T_M	3340 K
Liquidus temperature, T_L	3275 K
Eutectic temperature, T_E	3049 K
Specific heat, c_p	561 J kg^{-1} K
Thermal conductivity of solid, k_s	196 W m^{-1} K
Thermal conductivity of liquid, k_L	124 W m^{-1} K
Average density of solid powder, ρ	3384 kg m^{-3}

$$\left.\begin{aligned} &\text{at } z^* = 0, \quad \theta = \theta_i \\ &z^* = 1, \quad \frac{\partial\theta}{\partial z^*} = B_i[\theta(z^* = 1) - \theta_0] \end{aligned}\right\} \quad \tau > 0 \quad (28a)$$

$$\text{at } \tau = 0, \quad \theta = \theta_0 \quad \text{for } 0 \leqslant z^* \leqslant 1 \quad (28b)$$

The time–space temperature distribution in the combusting material was studied for parametric values of the left surface temperature θ_i, Biot number B_i, porosity p, non-reactive phase content v_f and the activation energy E for cases where the initial compact temperature has been assumed to be the ambient temperature θ_0.

4.1. Effect of left surface temperature, θ_i

After the left surface temperature was instantaneously brought to a sufficiently high temperature, θ_i, and was held constant, the temperature variations with non-dimensional time in the compact are shown in Figs 5–7. Here we have considered the material to be of zero porosity and the Biot number has been fixed at 1. The general pattern of temperature distribution clearly indicates that there is a certain amount of heating-up time associated with a competition between heat released in reaction and heat transfer characteristics. As intuitively expected, this heating up time is reduced when θ_i is increased, resulting in steeper temperature profiles at higher θ_i. After the temperature at nodes neighbouring the ignited left node attain a sufficiently high temperature, the exothermic reaction starts generating enough heat so that the reaction becomes self-sustaining and the front propagates through the mass. As seen in these figures,

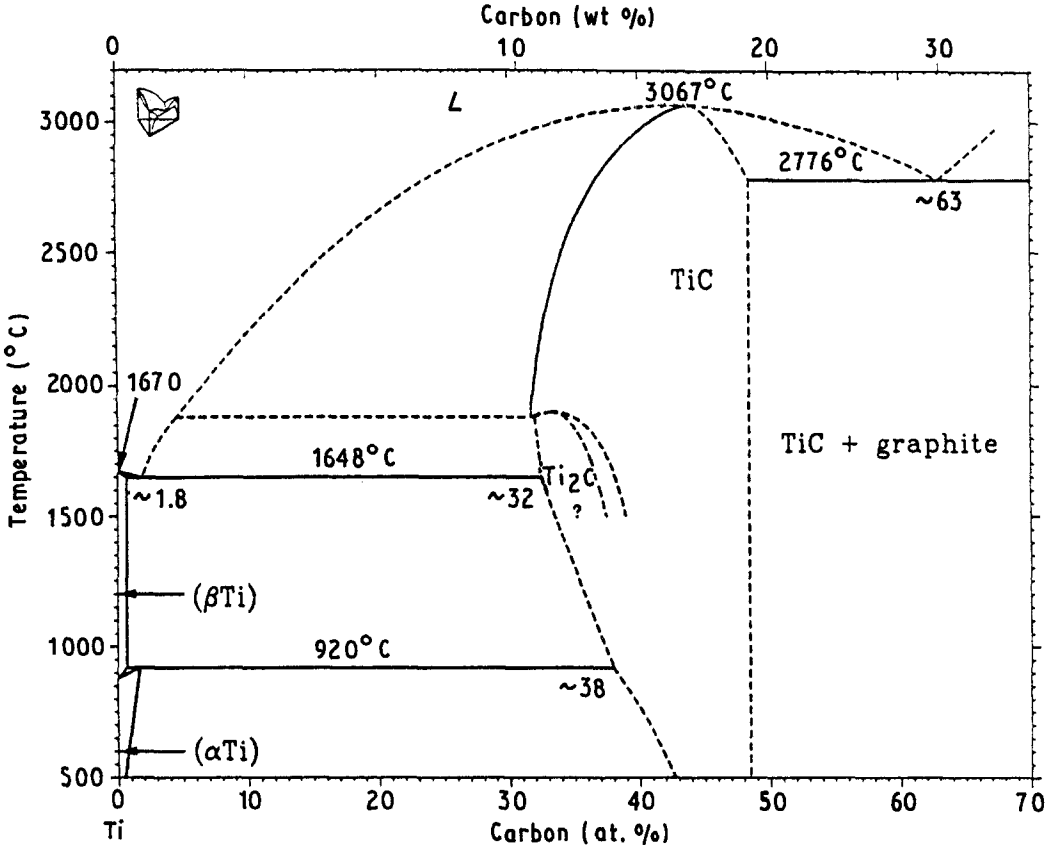

Figure 4 Binary phase diagram for Ti–C system [18].

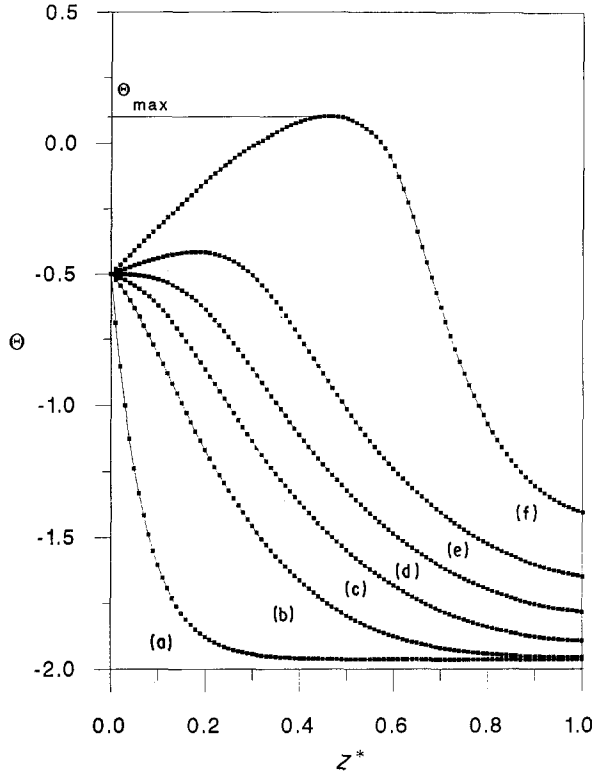

Figure 5 Time–space temperature profiles for fully dense compact ($\theta_i = -0.5$, $B_i = 1$, $p = 10\%$) at τ = (a) 0.005; (b) 0.05; (c) 0.1; (d) 0.15; (e) 0.2; (f) 0.25.

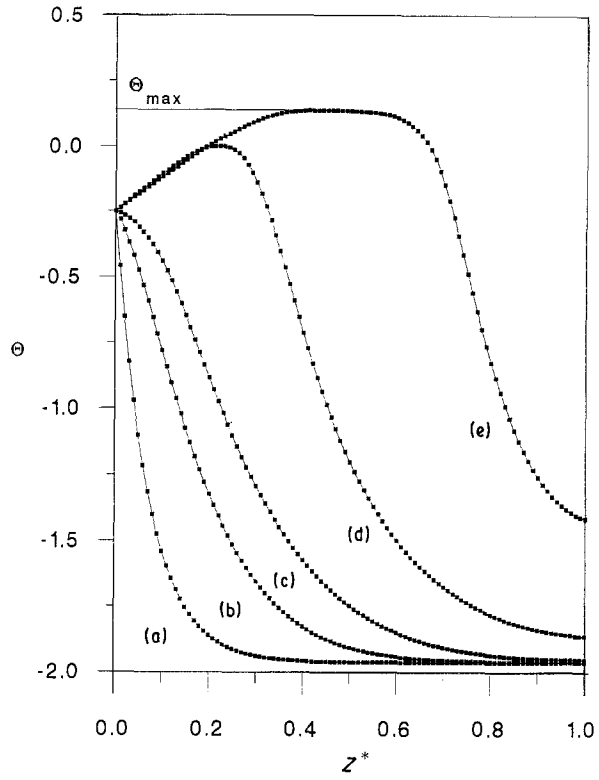

Figure 6 Time–space temperature profiles for fully dense compact ($\theta_i = -0.25$, $B_i = 1$, $p = 0$) at τ = (a) 0.005; (b) 0.025; (c) 0.05; (d) 0.1; (e) 0.15.

the maximum temperature is achieved somewhere inside the domain. This is partly a consequence of artificially restraining the left node temperature at a constant value, and partly because there is no heat loss from the left surface. However, changing the left node condition would not affect the overall pattern of temperature profiles. It is interesting to note that the maximum temperature θ_{max} achievable in the combustion process remains more or less the same, irrespective of the hold temperature at the left surface. The

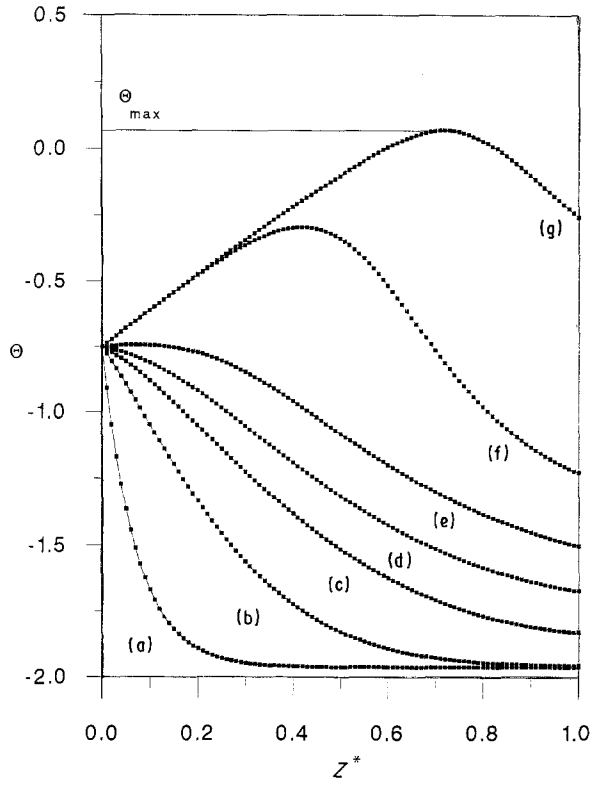

Figure 7 Time–space temperature profiles for fully dense compact ($\theta_i = -0.75$, $B_i = 1$, $p = 0$) at τ = (a) 0.005; (b) 0.05; (c) 0.15; (d) 0.25; (e) 0.375; (f) 0.5; (g) 0.75.

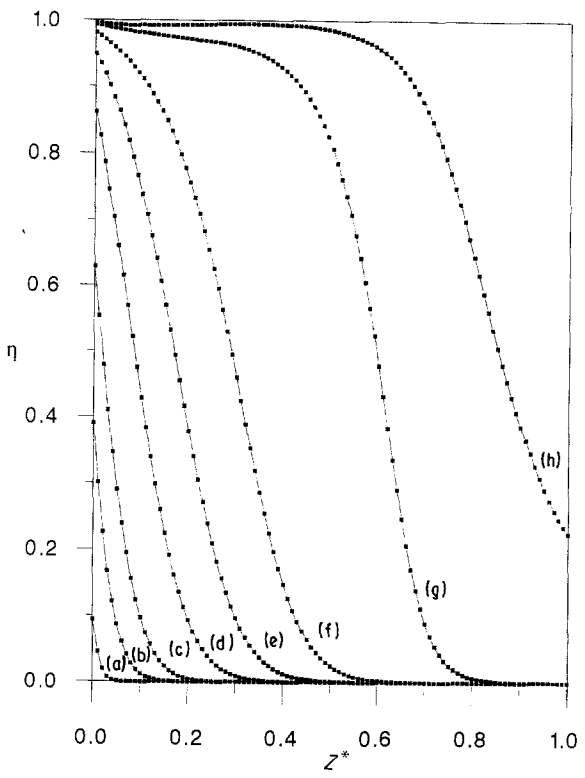

Figure 8 Time–space reaction conversion profiles ($\theta_i = -0.5$, $B_i = 1$, $p = 0$) for fully dense compact at τ = (a) 0.005; (b) 0.025; (c) 0.05; (d) 0.1; (e) 0.15; (f) 0.2; (g) 0.25; (h) 0.275.

most important observation in these plots is that, once the ignition process starts and the front begins to move, the velocity of propagation continues to increase as the front sweeps through the domain. Evidently this behaviour in a compact with zero porosity signifies an unsteady combustion process (non-constant pattern profile) with a continually increasing combustion velocity. Fig. 8 is a representative reaction-concentration profile for $\theta_i = -0.5$ and $B_i = 1$. Since η and θ are closely coupled in nature, we observe η to behave in a similar way as θ. This also acts as a verification of the numerical scheme used in the calculations.

4.2. Effect of Biot number B_i

The calculation procedure was also tested on problems where the convective heat transfer characteristics at the right surface of the material with zero porosity were varied by maintaining a fixed value of $\theta_i = -0.5$. The results of these calculations are shown in Figs 9 and 10 for $B_i = 0.1$ and 10, respectively. The temperature profiles (Figs 5, 9 and 10) are as expected, and show that the propagation process is strongly affected by the heat-transfer boundary condition on the free surface. As the Biot number increases, we observe a considerable slowing down in the propagation behaviour, although the combustion still becomes unsteady at lower Biot numbers ($B_i = 0.1$ and 1). However, it seems that for a very high Biot number ($B_i = 10$) the propagation process tends toward being stable. This indicates that, even for a compact with zero porosity, the combustion process in this material

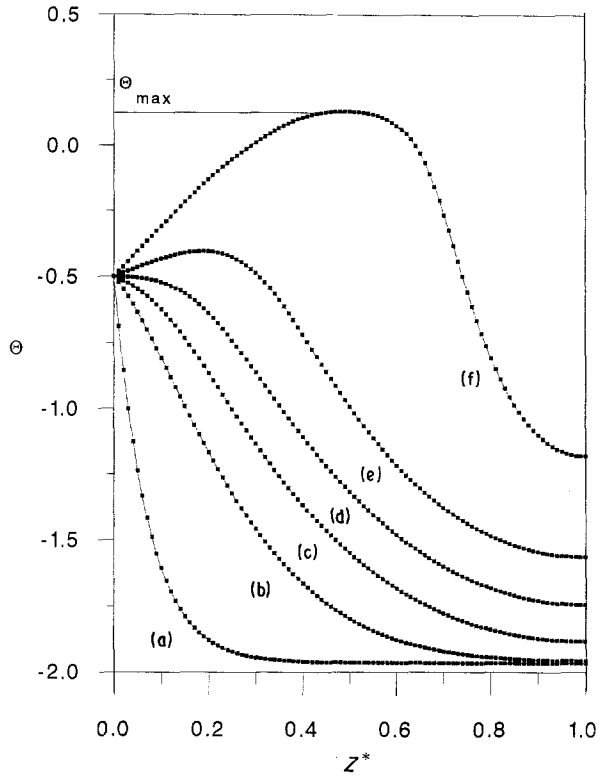

Figure 9 Effect of free surface heat loss on the time–space temperature profiles ($\theta_i = -0.5$, $B_i = 0.1$, $p = 0$) at τ = (a) 0.005; (b) 0.05; (c) 0.1; (d) 0.15; (e) 0.2; (f) 0.25.

can be stabilized by substantially increasing the heat loss characteristics at the remote free surface. Closer observation of Figs 5, 9 and 10 also indicates a large effect of the Biot number on the maximum achievable

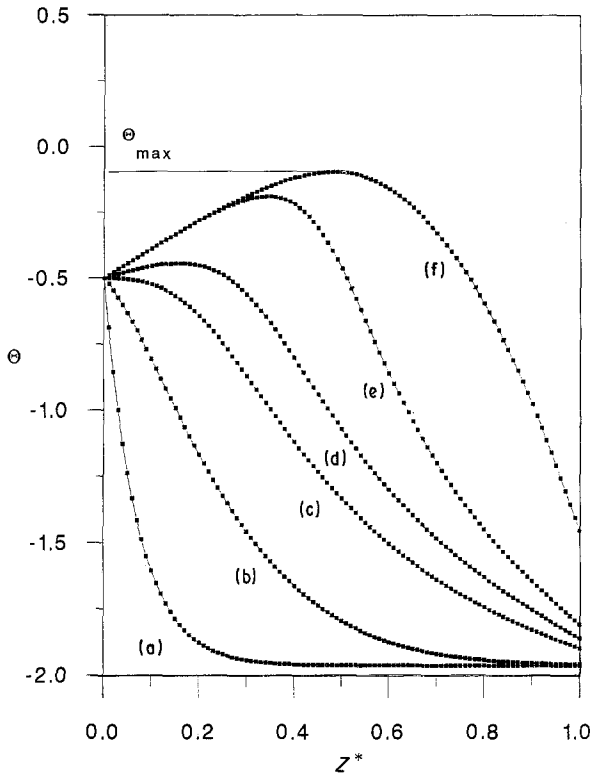

Figure 10 Effect of free surface heat loss on the time–space temperature profiles ($\theta_i = -0.5$, $B_i = 10$, $p = 0$) at τ = (a) 0.005; (b) 0.05; (c) 0.15; (d) 0.2; (e) 0.25; (f) 0.375.

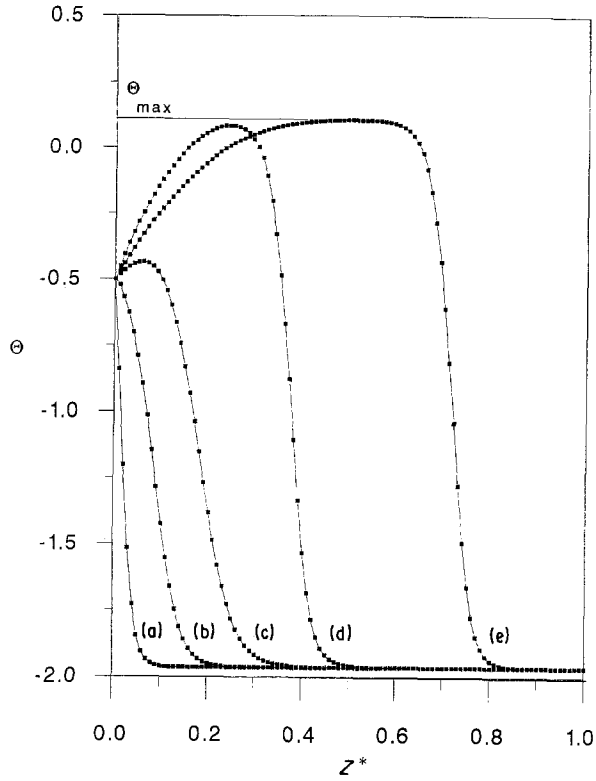

Figure 11 Effect of porosity ($p = 10\%$) on the time–space temperature profiles ($\theta_i = -0.5$, $B_i = 1$, $p = 10\%$) at τ = (a) 0.005; (b) 0.05; (c) 0.15; (d) 0.2; (e) 0.25.

combustion temperature, resulting in a reduction of θ_{max} at high Biot number.

4.3. Effect of porosity, p

Figs 11–13 show the effect of porosity on the combustion characteristics when we have considered fixed values of $B_i = 1$ and $\theta_i = -0.5$. Compared to zero porosity we now observe a distinctly different behaviour. The temperature profiles are now much steeper for all porosity levels. This indicates a narrow reaction zone around the combustion front. Similar behaviour is also observed in the concentration profiles shown in Fig. 14 for a typical porosity level of 25%. This behaviour gives rise to a stable and constant velocity profile for all porosities. This change in pattern is primarily due to the influence of local thermal conductivity on the heat transfer process. As seen in Equation 20, the overall thermal conductivity is considerably reduced with the increase in porosity. This is to be expected in a porous compact, because all of the pores (assumed to contain air) now act as insulating devices with regard to the local heat transfer process. The local exothermic reaction, however, continues and thus become localized around a narrow zone in the material. Also, the maximum combustion temperature and the combustion front velocity gradually decrease with the increase in porosity. This prediction is consistent with experimental observations by various authors [19, 20] on different materials. In these calculations we have considered the pore size parameter Ω to be 0.1 which, for this material system, reflects an average pore size of 14 μm. This order of

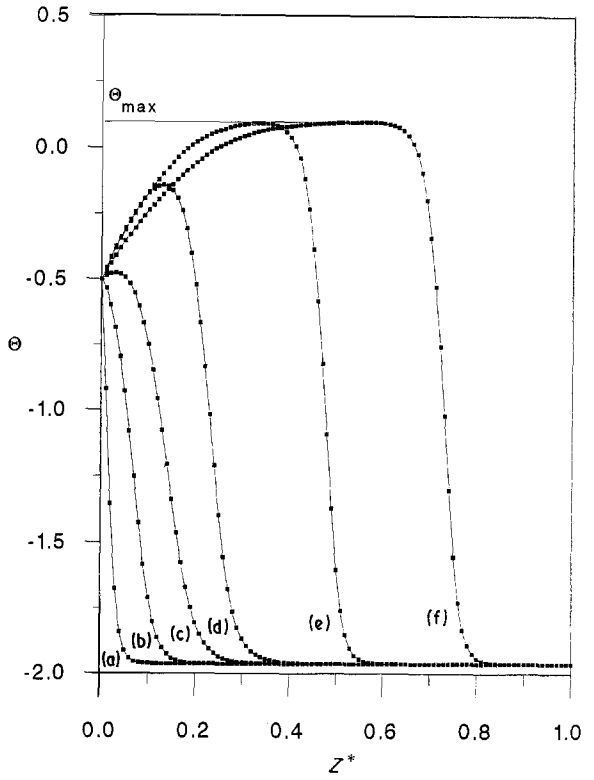

Figure 12 Effect of porosity ($p = 25\%$) on the time–space temperature profiles ($\theta_i = -0.5$, $B_i = 1$, $p = 25\%$) at τ = (a) 0.005; (b) 0.05; (c) 0.15; (d) 0.25; (e) 0.375; (f) 0.5.

value is typical for a particular compact used in combustion synthesis. In the present treatment we have not considered the effect of changing porosity on the resulting pore size. Under a constant compaction

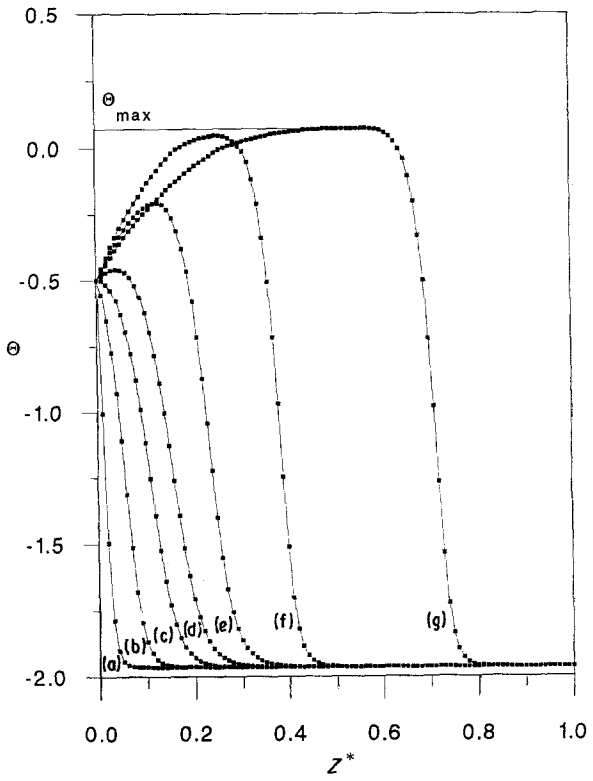

Figure 13 Effect of porosity ($p = 50\%$) on the time–space temperature profiles ($\theta_i = -0.5$, $B_i = 1$) at τ = (a) 0.005; (b) 0.05; (c) 0.15; (d) 0.25; (e) 0.375; (f) 0.5; (g) 0.75.

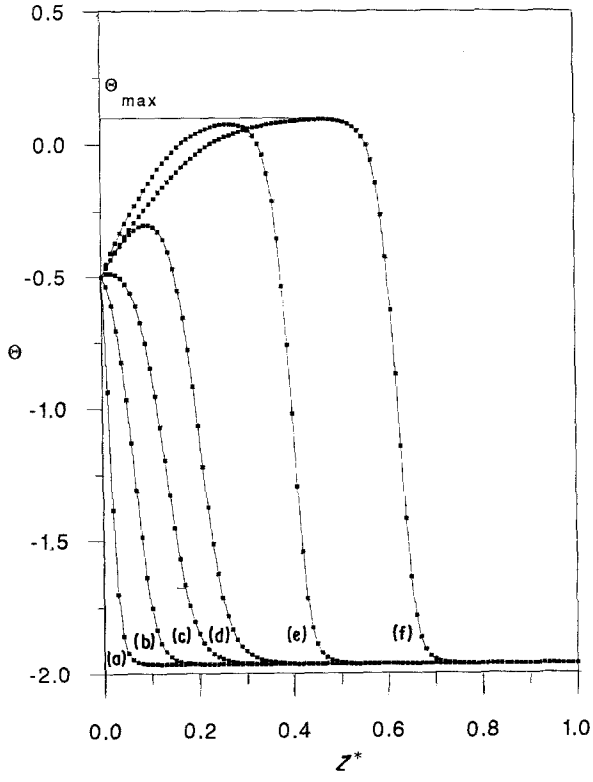

Figure 15 Effect of non-reacting compositing phase (10% SiC, $B_i = 1$) on the time–space temperature profiles in a 25% porous compact at τ = (a) 0.005; (b) 0.05; (c) 0.15; (d) 0.25; (e) 0.375; (f) 0.5.

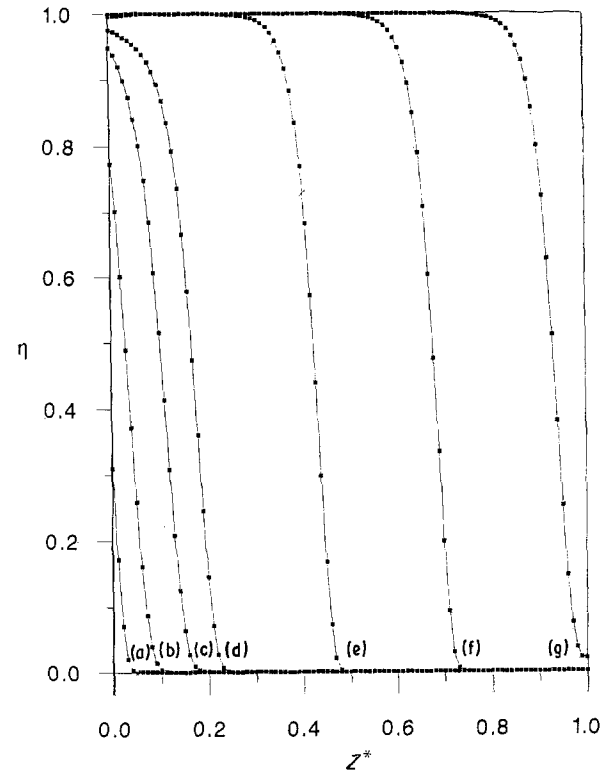

Figure 14 Time–space conversion profiles in a compact having 25% porosity ($\theta_i = -0.5$, $B_i = 1$) at τ = (a) 0.025; (b) 0.1; (c) 0.2; (d) 0.25; (e) 0.375; (f) 0.5; (g) 0.625.

pressure, it is reasonable to expect that to achieve different porosity, we will obtain different pore sizes in the resulting compact. An attempt has been made recently by the author [21] to treat this problem explicitly, although it has not been included here for the sake of simplicity in presenting results. However, it was found that for quite large pore sizes the local overall conduction process may even increase beyond that for solid conductivity due to enhanced contribution from radiation across the pore surfaces. Thus in such cases of large pores, the very steep temperature profiles in Figs 11–13 may revert back to those similar to the case with zero porosity (Fig. 5), resulting in an unsteady combustion front.

4.4. Effect of non-reacting reinforcement content, v_f

The model formulation is also capable of considering the effects of inert compositing phases which may be included while synthesizing ceramic or intermetallic composites. To demonstrate this, we have considered a synthesis of TiC + SiC composites from a powder mixture of Ti, C and SiC. Figs 15–17 show the temperature distribution for combusting a compact with a 25% porosity level, and the SiC content has been varied up to 30%. Solid density and the thermal conductivity of the compact has been calculated with due consideration of the SiC content. The model prediction indicates that the steady-state combustion is feasible in such a composite up to the maximum SiC content (30%) considered in these plots. However, as can be expected, the addition of non-reactive inert phase reduces the combustion velocity when compared to that for a material with same porosity and containing no inert phase. Also, the maximum combustion temperature gradually decreases as the SiC content is increased, which is to be expected as the inert phase acts as heat sinks and thus reduces both combustion temperature and velocity.

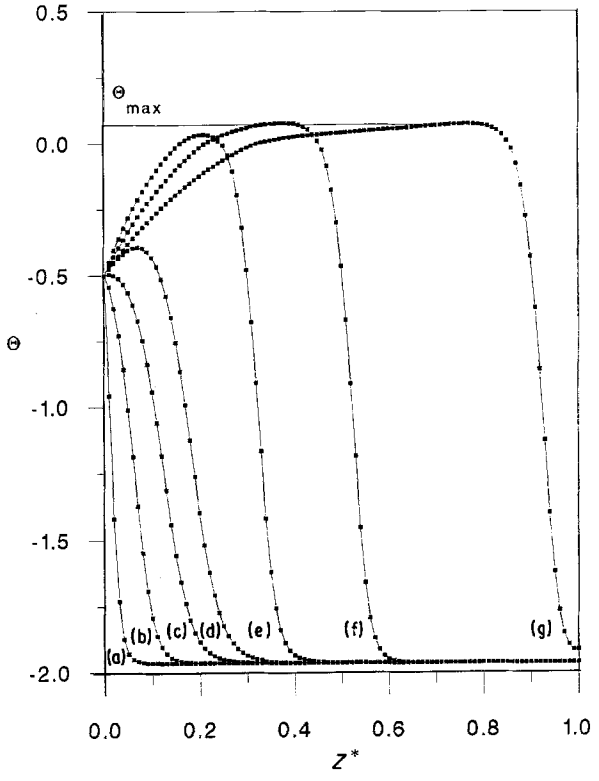

Figure 16 Effect of non-reacting compositing phase (20% SiC, $B_i = 1$) on the time–space temperature profiles in a 25% porous compact at τ = (a) 0.005; (b) 0.05; (c) 0.15; (d) 0.25; (e) 0.375; (f) 0.5; (g) 0.75.

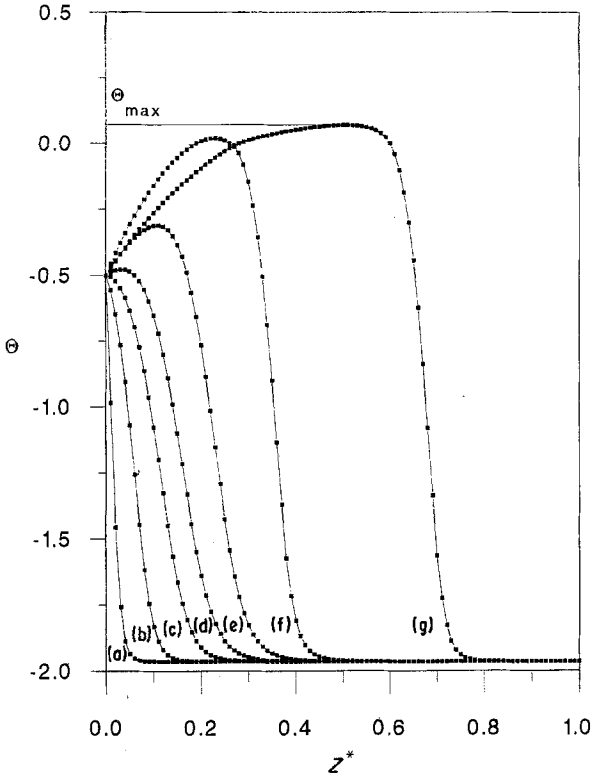

Figure 17 Effect of non-reacting compositing phase (30% SiC, $B_i = 1$) on the time–space temperature profiles in a 25% porous compact at τ = (a) 0.005; (b) 0.05; (c) 0.15; (d) 0.25; (e) 0.375; (f) 0.5; (g) 0.75.

4.5. Effect of activation energy, E

It has been observed experimentally [22] and also numerically analysed [10] that the activation energy

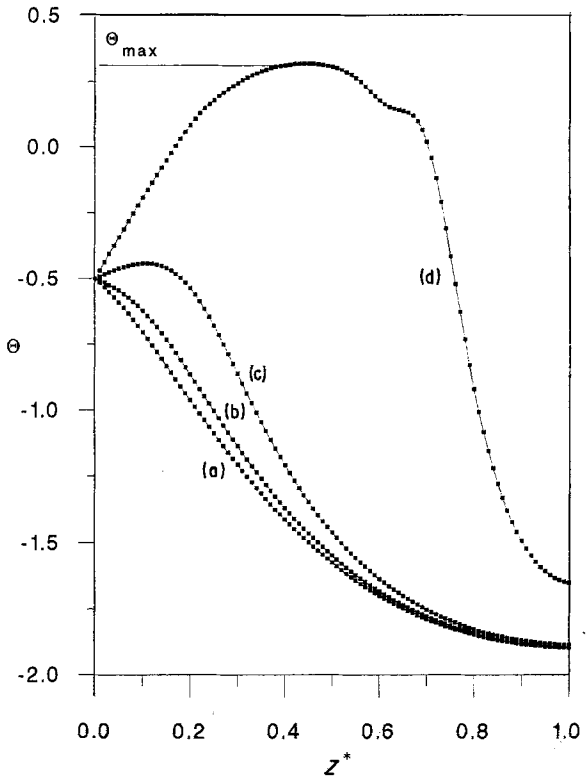

Figure 18 Effect of activation energy on the temperature profiles ($\theta_i = -0.5$, $p = 0$, $B_i = 1$, $E_{ref} = 117\ kJ\ mol^{-1}$) for E_{ref}/E = (a) 0.9; (b) 1.0; (c) 1.1; (d) 1.2.

plays a key role in deciding whether the combustion process will be stable or unstable. In a typical combustion process, compounds could form by solid-state or liquid-state reactions. Experimental studies by Holt and Munir [8] on the synthesis of TiC have shown that there could be a large range of activation energy depending on the actual composition of Ti and C which could determine the stable or unstable mode of combustion. Numerical analysis by Dimitriou *et al.* [10] also predicted a very sensitive dependence of activation energy on the stability of the wave front. In Fig. 18 we show the present model prediction of the effect of E on the temperature distribution at a fixed time $\tau = 0.1$. The value of E has been changed from $E_{ref}/E = 0.9$ to 1.2 where $E_{ref} = 117\ kJ\ mol^{-1}$ has been used for all other calculations. It is evident that E has a very strong effect on the combustion process, and the plot shows that by decreasing the activation energy it is possible to reach a higher combustion temperature in less time, which gives rise to increased combustion velocity.

4.6. Steady-state combustion velocity

Finally, we present the variation of non-dimensionalized steady-state combustion velocity with porosity, and also the SiC content, in Fig. 19. The velocity is calculated as $V^* = \Delta z^*/\Delta\tau$ in the steady-state regime of the appropriate domains. The left vertical axis represents percentage porosity values of a compact, and the right vertical axis indicates the percentage SiC content in the composite with 25% porosity. As seen in the plot, the velocity V^* quickly drops by increasing the porosity level from 10 to 15%. The rate of this drop gradually slows down and it appears that it

reaches some constant velocity at very large porosity level. It is interesting to note here that the combustion process gives rise to a steady-state propagation for 10% porosity although the front velocity is quite high in this case. However, we have seen earlier in Figs 5–7 that the compacts with zero porosity give rise to continually increasing combustion velocity, which indicates unsteady propagation. This clearly signifies the important role of porosity in the combustion heat-transfer phenomena. A decrease in combustion velocity with increasing porosity, as we observe here, has been experimentally observed by various researchers [19, 20].

On the other hand, by increasing the SiC content from 0% at a fixed porosity level of 25%, the reduction in velocity is gradual and it is observed that at an extrapolated value of 47% SiC content, the propagation velocity reduces to zero. This signifies that at this level of reinforcement, the combustion process will possibly lead to extinction. We have only indicated results for 25% porosity and its SiC composite for illustration. However, TiC–SiC composites having, say, 40–50% porosity (which is a typical green compact porosity), will give rise to lower combustion velocity and also the limiting extinction will take place at a lower SiC content.

In all of the above calculations, the description of the various reacted phases at a particular time and location are directly obtainable as natural by-product of this formulation. These calculations may include solid and liquid content if the material is in the mushy or in the liquid phase. This permits us to be able to draw appropriate "phase maps" evolving with time. A detailed discussion on this aspect will be the subject matter of a later report.

5. Conclusions

A powerful temperature–enthalpy model has been developed to analyse self-propagating high-temperature combustion synthesis. This technique has been demonstrated to be particularly useful in considering the various aspects of phase change that take place during the combustion process. It is also demonstrated how the important effect of green compact porosity can be adopted in such an analysis. The model equations have been solved by a finite difference technique, and the various important parametric effects have been studied. These results indicate that the model can predict the conditions for steady-state propagation under various operating conditions. Also, the maximum combustion temperature under these conditions is automatically obtained from these simulated results. It is seen that decreasing compact porosity level increases combustion wave velocity. Also, the model successfully predicts that by increasing the content of non-reacting species, the combustion wave velocity gradually decreases, eventually leading to extinction of the combustion process. It is also seen that the boundary condition can significantly alter the propagation behaviour in a fully dense compact and thus, by increasing the heat-loss condition to a high value, the wave propagation can change from unsteady to steady behaviour. All these predictions from the model are in close agreement with experimentally observed trends.

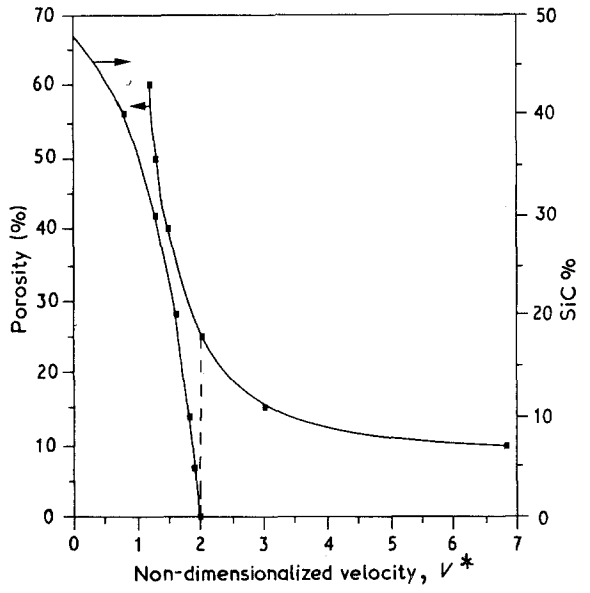

Figure 19 Dependence of non-dimensional steady state combustion velocity on the porosity of compact and non-reacting compositing phase (SiC) content.

References

1. B. V. NOVOZHILOV, *Dokl. Akad. Sci. USSR, Phys. Chem.* (English Translation) **141** (1961) 151.
2. A. G. MERZHANOV and I. P. BOROVINSKAYA, *ibid.* **204** (1972) 429.
3. O. R. BERGMAN and J. BARRINGTON, *J. Amer. Ceram. Soc.* **49** (1966) 502.
4. W. L. FRANKHAUSER, K. W. BRENDLY, M. C. KIESZEK and S. T. SULLIVAN, "Gasless Combustion Synthesis of Refractory Compounds" (Noyes Publications, New Jersey, 1985).
5. Z. A. MUNIR, *Amer. Ceram. Soc. Bull.* **67** (1988) 342.
6. A. G. MERZHANOV and B. I. KHAIKIN, *Prog. Energy Comb. Sci.* **14** (1988) 1.
7. H. C. YI and J. J. MOORE, *J. Mater. Sci.* **25** (1990) 1159.
8. J. B. HOLT and Z. A. MUNIR, *ibid.* **21** (1986) 251.
9. J. PUSZYNSKI, J. DEGREVE and V. HLAVACEK, *Ind. Engng Chem. Res.* **26** (1987) 1424.
10. P. DIMITRIOU, J. PUSZYNSKI and V. HLAVACEK, *Comb. Sci. Tech.* **68** (1989) 101.
11. G. M. DUSINBERRE, *Trans. ASME* **67** (1945) 703.
12. S. KOU, S. C. HSU and R. MEHRABIAN, *Met. Trans.* **12B** (1981) 33.
13. J. A. SEKHAR, G. J. ABBASCHIAN and R. MEHRABIAN, *Mat. Sci. Engng* **40** (1979) 105.
14. B. BASU and J. A. SEKHAR, *Met. Trans.* **20A** (1989) 1833.
15. M. C. FLEMINGS, "Solidification Processing" (McGraw Hill, New York, 1974).
16. A. K. BHATTACHARYA, *J. Amer. Ceram. Soc.* **74** (1991) 2113.
17. D. A. ZUMBRUNNEN, R. VISKANTA and F. P. INCROPERA, *Int. J. Heat Mass Trans.* **29** (1986) 275.
18. T. B. MASSALSKI (ed.), "Binary Alloy Phase Diagrams", Vol. 1 (ASM, 1986).
19. T. S. AZATYAN, V. M. MAL'TSEV, A. G. MERZHANOV and V. A. SELEZNEV, *Comb. Explos. Shock Wave* **15** (1979) 35.
20. R. W. RICE, G. Y. RICHARDSON, J. M. KUNETZ, T. SCHROETER and W. J. McDONOUGH, *Ceram. Engng Sci. Proc.* **7** (1986) 736.
21. A. K. BHATTACHARYA, *J. Mater. Sci.* In the press.
22. S. D. DUNNMEAD, D. W. READEY, C. E. SEMLER and J. B. HOLT, *J. Amer. Ceram. Soc.* **72** (1989) 2318.

Received 7 February
and accepted 25 July 1991